J. Fluid Mech. (2012), *vol.* 691, *pp.* 245–266.
doi:10.1017/jfm.2011.472

On the relationship between efficiency and wake structure of a batoid-inspired oscillating fin

Peter A. Dewey[1]†, Antoine Carriou[2] and Alexander J. Smits[1]

[1] Department of Mechanical and Aerospace Engineering, Princeton University, Princeton, NJ 08544, USA

[2] Department of Engineering, École Supérieure de Physique et de Chimie Industrielles, Paris, France

(Received 25 May 2011; revised 25 September 2011; accepted 20 October 2011; first published online 5 December 2011)

A mechanical representation of batoid-like propulsion using a flexible fin with an elliptical planform shape is used to study the hydrodynamics of undulatory propulsion. The wake is found to consist of a series of interconnected vortex rings, whereby leading and trailing edge vortices of subsequent cycles become entangled with one another. Efficient propulsion is achieved when leading and trailing edge vortices coalesce at the spanwise location where most of the streamwise fluid momentum is concentrated in the wake of the fin. Both the Strouhal number and the wavelength are found to have a significant effect on the wake structure. In general, a decrease in wavelength promotes a wake transition from shedding a single vortex per half-oscillation period to shedding a pair of vortices per half-oscillation period. An increase in Strouhal number causes the wake to bifurcate a finite distance downstream of the trailing edge of the fin into a pair of jets oriented at an acute angle to the line of symmetry. The bifurcation distance decreases with increasing Strouhal number and wavelength, and it is shown to obey a simple scaling law.

Key words: propulsion, swimming/flying, vortex dynamics

1. Introduction

Aquatic animals have garnered much attention for the development of bio-inspired underwater vehicles, in that many display high manoeuvrability, rapid acceleration, and a level of endurance unmatched by current man-made devices. Here, we aim to describe more clearly the nature of three-dimensional unsteady wakes associated with undulatory swimmers. We specifically focus our attention on the manta ray, a batoid fish that employs large dorsoventrally flattened pectoral fins for propulsion (Rosenberger 2001). Batoid species – particularly the manta ray, the largest animal in the family with tip-to-tip sizes up to 5–6 m – have the ability to keep station, develop bursts of high acceleration, swim at speeds up to 10 m s^{-1}, and are presumed to be efficient swimmers due to their long range capabilities and pectoral fin kinematics (Walker & Westneat 2002). Rays flap their fins much in the same way as birds flap their wings while flying, although the lift generated is principally for thrust and not for depth control as the animal is only slightly negatively buoyant. In addition to this

† Email address for correspondence: pdewey@princeton.edu

baseline flapping motion, a hallmark of ray swimming is the presence of a chordwise travelling wave motion, which has been shown to be a highly effective propulsive mechanism (Clark & Smits 2006). Much of our attention will focus on the effect of this chordwise travelling wave, and while our study focuses on the manta ray pectoral fin, similarities can be drawn to other aquatic animals that utilize undulatory motions of their body (or other fins) for propulsion.

The characteristics of unsteady propulsion are known to vary with Reynolds number, $Re = UL/\nu$, and the Strouhal number, $St = fA/U$, where U is the swimming speed or free-stream velocity, L is a characteristic length scale (the length of the fish, or the fin chord length), ν is the kinematic viscosity of the fluid, f is the frequency of fin oscillation, and A is the width of the wake (usually approximated by the peak-to-peak lateral excursion of the fin). As long as the Reynolds numbers exceed $\approx 10^4$, the Strouhal number effects tend to dominate the propulsive performance due to the high degree of unsteadiness of the flow (Buchholz & Smits 2008).

In two dimensions, Triantafyllou, Triantafyllou & Gopalkrishnan (1991) and Triantafyllou, Triantafyllou & Grosenbaugh (1993) used a linear spatial stability analysis to show that the flapping frequency of an oscillating foil matched the most unstable spatial mode of the velocity profile for $St \approx 0.25$–0.35. It was suggested that swimming in this regime would be efficient because the oscillating foil (or fish fin) would exploit the resonant instability of the wake. Their conclusion was supported by observations on the swimming gaits of various animals in nature (Taylor, Nudds & Thomas 2003), as well as the experimental study by Anderson *et al.* (1998) and the computational findings of Guglielmini & Blondeaux (2004), where efficiencies were found to peak near $St = 0.25$.

A qualitative assessment of the wake structure of an oscillating foil suggests that efficient propulsion results in the shedding of a pair of vortices per oscillation cycle that align themselves in a staggered array similar to a von Kármán vortex street, but with the sense of rotation of the vortices reversed, known as a reverse von Kármán vortex street. The rotation of the vortices induces velocities that increase the streamwise component of momentum and are thus related to thrust production. When viscous effects, governed by the Reynolds number, result in leading edge separation, Anderson *et al.* (1998), Lewin & Haj-Hariri (2003) and Guglielmini & Blondeaux (2004) have demonstrated that efficiency curves display a peak when the leading edge vortices constructively interfere with the trailing edge vortices to form a reverse von Kármán vortex street.

If the leading edge and trailing edge vortices are not in phase, more complex wakes are observed with multiple vortices shed per half-oscillation cycle. Williamson & Roshko (1988), in a study of transversely oscillating cylinders, classified the wake structures based on the number of vortices shed in a single period. Using this convention, a wake with a single vortex shed per half-oscillation cycle is denoted 2S (two single vortices shed per period) and a wake with a pair of vortices shed per half-oscillation cycle is denoted 2P (two pairs of vortices shed per period). Similar wake patterns were observed behind a pitching aerofoil by Koochesfahani (1989). More recently, Lentink *et al.* (2008) and Schnipper, Andersen & Bohr (2009) examined the flow past flapping foils in soap-film experiments and observed flow cases that included 4P to 8P wakes.

Transitions from 2S to 2P wakes have also been seen with decreasing oscillation frequency (Williamson & Roshko 1988; Koochesfahani 1989; Lentink *et al.* 2008; Schnipper *et al.* 2009). Here, the characteristic time of an oscillation period increases, suggesting that the formation number may be an important parameter. The formation

number, introduced by Gharib, Rambod & Shariff (1998) and recently reviewed by Dabiri (2009), is defined by

$$\hat{T} = \frac{C\Gamma}{D\Delta U}. \tag{1.1}$$

Here, Γ is the instantaneous vortex circulation, ΔU and D are the characteristic shear layer velocity and length scale respectively, and the constant C is based on the physical configuration of the vortex generator and the inverse of the dimensionless vorticity flux $\mathrm{d}\hat{\Gamma}/\mathrm{d}\hat{T}$.

It has been proposed that after a sufficient non-dimensional time (that is, when $\hat{T}$ reaches a specific value that is typically 4), the vortex formation reaches saturation and a trailing shear-layer-like structure is then created. It may be a more robust parameter than the Strouhal number in cases where the Strouhal number is difficult to define (for example, when the amplitude is changing with spanwise location, or when $U = 0$). The formation number concept has been extended to flows past oscillating cylinders by Jeon & Gharib (2004), to temporarily varying orifices by Dabiri & Gharib (2005), and to oscillatory plates of finite-aspect ratio in a quiescent fluid by Milano & Gharib (2005). It should be noted, however, that studies examining formation number have primarily been limited to two-dimensional or axisymmetric flows, whereas the wakes seen in biological propulsion are generally highly three-dimensional.

Three-dimensional wakes are fundamentally different from two-dimensional wakes. For example, the wake generated by a finite-aspect-ratio foil is characterized by interlinked vortex rings generated by the interactions of spanwise and trailing edge vortices. von Ellenrieder, Parker & Soria (2003) used flow visualization experiments to develop a three-dimensional vortex model for a heaving and pitching foil of aspect ratio 3 at $Re = 164$, $St = 0.2$–0.4. The model presents a series of interconnected vortex rings made up of contributions from leading edge and trailing edge vortices, where a single vortex ring is shed per half-flapping cycle with the subsequent vortex rings being of opposite sign. Computations for an identical setup by Blondeaux *et al.* (2005) found a similar vortex structure.

Buchholz & Smits (2006, 2008) and Green & Smits (2008) examined the three-dimensional wakes and pressure distributions generated by a rigid pitching panel with aspect ratios ranging from 0.54–2.38. For $Re = O(10^3)$ and $St < 0.25$, a wake skeleton was presented consisting of a series of interconnected vortex rings formed from horseshoe vortices shed from the edges of the rectangular panel, similar to the model presented by von Ellenrieder *et al.* (2003). For increasing Strouhal number, however, the spanwise vorticity begins to reorganize, and a wake model presented for $St = 0.43$ suggests the creation of vortex rings that move by self-induction away from the line of symmetry of the pitching panel and lead to a wake bifurcation. Interestingly, the propulsive efficiency curve (defined as the ratio of the thrust times the velocity to the power delivered to the fluid by the panel) displays a peak at a Strouhal number just below that of the bifurcation point where the wake transitions from a 2S to a 2P wake structure. This result highlights a fundamental difference between two-dimensional and three-dimensional flows: with increasing Strouhal number two-dimensional heaving foils yield asymmetric 2S wakes (Lewin & Haj-Hariri 2003; Godoy-Diana, Aider & Wesfreid 2008; Godoy-Diana *et al.* 2009), whereas finite-aspect-ratio foils yield symmetric 2P wakes. Despite important differences in the wake structure of two and three-dimensional wakes, efficiency curves for both types of wakes display similar trends with peak efficiencies occurring near $St = 0.25$.

Bifurcating wakes have also been observed computationally by Dong, Mital & Najjar (2006) who employed an immersed boundary method to examine how Strouhal number, Reynolds number, and aspect ratio of an elliptical foil were related to performance. With decreasing aspect ratio, the wake remained symmetric but bifurcated into a double wake structure consisting of pairs of a vortex rings. The bifurcation, when time-averaged, resulted in the formation of a velocity jet existing at an acute angle to the line of symmetry. This angle was seen to increase with decreasing aspect ratio, whereas efficiencies increased with increasing aspect ratio.

Similar phenomena are widely found in nature. For instance, Drucker & Lauder (1999) observed the creation of vortex rings similar to those seen by Dong *et al.* (2006) on the pectoral fin of swimming fish. Borazjani & Sotiropoulos (2008) performed computational simulations of a mackerel-like model fish and also observed bifurcating wakes with increasing Strouhal number. In addition, Tytell & Lauder (2004) and Hultmark, Leftwich & Smits (2007) found that anguilliform swimmers (American eels and a mechanical lamprey, respectively) generate 2P wake structures representative of bifurcating wakes for all Strouhal numbers examined.

Here, we are particularly interested in undulatory swimming as seen in rays. The first hydrodynamic study in this area was done by Clark & Smits (2006) who studied the propulsive efficiencies and wake structures of a batoid-inspired oscillating fin for $Re = 11\,400$. To replicate batoid propulsion, the amplitude of oscillation was linearly increased from the root to the tip of the fin, and a streamwise travelling wave motion was thereby induced along the chord of the fin. It was found that the maximum efficiency occurred for a wavelength 4–6 times the length of the chord at $St \approx 0.25$. Flow visualizations revealed a wake structure consisting of interconnecting vortex tubes generated from the trailing edge of the fin. The spanwise extent of these tubes decreased downstream of the fin, a result in accordance with the observations by Buchholz & Smits (2006) and Dong *et al.* (2006).

In the current study, we extend the work of Clark & Smits (2006) by performing a detailed analysis of the vortex structures in the wake of a batoid-inspired oscillating fin. Although the exact kinematic motion of batoid fins is unknown, it is known that the animal couples two principal motions of their flexible pectoral fins as a propulsive mechanism: oscillatory flapping with spanwise curvature, and a chordwise travelling wave component (Heine 1992; Rosenberger 2001; Schaefer & Summers 2005). The wavelength λ varies between species, with some displaying wavelengths longer than the fin chord length C (manta rays) and some with wavelengths shorter than the fin chord length (Atlantic stingrays). Here, we examine the wake structures that lead to efficient propulsion in the case where $\lambda > C$. In particular, we focus on the effect that the Strouhal number and wavelength have on the three-dimensional vortex structures that relate to propulsion and efficiency, in order to gain further insight into the three-dimensional kinematic motions generated by flexible oscillating fins and their resulting wakes. Note that owing to limitations in our experimental setup, we do not employ the formation number analysis in this work; in the conclusions we address its scope for work presently under investigation.

2. Experimental methods

The experimental arrangements closely follow those originally used by Clark & Smits (2006). To create kinematic motion similar to that seen in rays, an elliptical planform fin with an aspect ratio of 0.9 and a NACA 0020 cross-section was cast using a flexible PVC plastic (MF Manufacturing). The root chord of the fin measured

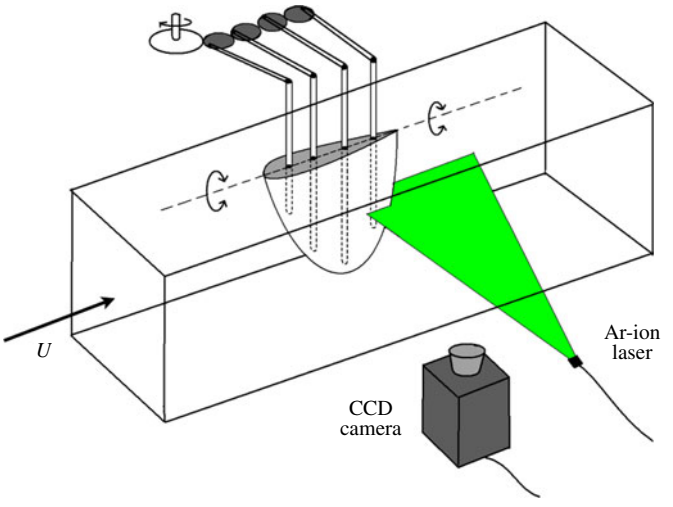

FIGURE 1. (Colour online available at journals.cambridge.org/flm) Experimental setup. DPIV was taken in the wake of the fin at 10 different spanwise locations ranging from the tip to the midspan of the fin.

0.24 m and the span measured 0.215 m. Aluminium spars were embedded into the fin to achieve actuation and were spaced 0.05 m apart with the first spar 0.05 m from the leading edge and the last spar 0.04 m from the trailing edge. The spar diameter was 0.00635 m and extended 0.12, 0.19, 0.19 and 0.1 m into the fin for the first (leading edge), second, third, and fourth (trailing edge) spars, respectively. The actuation spars embedded into the fin were set into motion using a DC motor coupled to a gear train, as illustrated in figure 1. A push-rod connected each spar to a gear in a gear train driven by a DC motor (Pittman GM-9236S015-R1), which upon rotation produces a sinusoidal rotation of the spar about a pivot point located at the root chord of the fin. The amplitude of the motion linearly increased along the span of the fin S, and by introducing constant phase differences in the actuation of adjacent spars, a travelling wave was generated that moved from the leading to the trailing edge along the chord. The phase difference is directly related to the wavelength λ of the travelling wave, usually expressed non-dimensionally as $\lambda^* = \lambda/C$, where C is understood to be the chord length at midspan. The rotational speed of the motor, and thus the fin flapping frequency, was determined using a digital optical encoder on the motor.

The apparatus was mounted in a closed-loop, free surface water channel having a test section 0.46 m wide, 0.3 m deep, and 2.44 m long with free-stream turbulence intensity less than 3 % at the Reynolds numbers of interest. The chord of the fin was aligned with the free-stream direction and the root chord was set at the free surface. An acrylic plate was mounted at the root chord of the fin, extending 0.1 m upstream and 0.4 m downstream of the fin, to minimize surface waves and to approximate a plane of symmetry. Although the span of the fin protruded 70 % of the depth of the channel, no particular wall effects were observed. The blockage ratio of the inactive fin in the water channel was small (2.8 %) in the hope of minimizing any flow distortion due to its presence. The experimental conditions are summarized in table 1. The chord Reynolds number was held constant at $Re_C \approx 11\,600$ unless otherwise noted. The non-dimensional amplitude, A/C, is based on the peak-to-peak amplitude

AR	*Re*	*A*/*C*	λ^*	*St*
0.9	8100, 11 600	0.125	2.4, 3, 4 6, 12 ∞	0.1–0.65 (by 0.025 increments)

TABLE 1. Experimental conditions.

at the midspan of the fin. The Strouhal number is also defined using the peak-to-peak amplitude of the trailing edge of the fin at the midspan of the fin.

Digital particle image velocimetry (DPIV) data were acquired with a Spectra Physics 2020 continuous wave Argon-Ion laser and Redlake MotionXtra HG-LE 8-bit monochrome CCD camera with 1128 × 752 pixel resolution (see figure 1). A Powell lens (Oz Optics Ltd.) was used in conjunction with a beam collimator and fibre optic cable to deliver a 1.5 mm thick laser sheet. The discrete phases of the flapping cycle were determined using a timing-control system (Stanford Research Systems DG535) that was triggered by a Hall-effect sensor attached to the leading edge spar of the fin. The sensor triggered the DPIV system once per flapping cycle to acquire an image pair at a pre-determined phase in the flapping cycle. Each oscillation period was divided into 30 equally spaced discrete phases for this study. The flow was seeded with neutrally buoyant silver coated hollow ceramic spheres with a mean diameter of 93 μm (Potters Industries Inc. Conduct-O-Fil AGSL150 TRD).

Data were acquired at ten different spanwise locations z/S, ranging from the tip to the midspan of the fin. Two-dimensional velocity fields were computed by calculating local spatial cross-correlations using software developed by Jiménez (2002). Two passes, with window sizes of 64 × 64 and 32 × 32 pixel windows with 50 % overlap, were made over the interrogation region yielding vectors spaced 16 pixels apart, corresponding to ∼60 velocity vectors per chord length. To achieve sub-pixel accuracy, a 5 × 5 pixel Gaussian interpolation was performed. The velocity data set consisted of 44 × 67 = 2948 points per phase in the oscillation cycle for a total of 2948 × 30 = 88 440 data points per oscillation period. The vorticity was calculated at each point by computing the circulation about a closed contour formed by the 8 neighbouring points using a trapezoidal rule scheme (Raffel, Willert & Kompenhans 1998). Tests by Chan *et al.* (2011) gave an estimated uncertainty of 1–5 % in the velocity and 5–10 % in the vorticity.

3. Effects of wavelength

Here we discuss the results obtained for different wavelengths of the travelling wave motion, λ^*, at a fixed Strouhal number of $St = 0.25$.

Figure 2 shows streamwise vorticity fields and figure 3 shows time-averaged velocity fields for four different spanwise locations extending from the midspan to the tip of the fin for $\lambda^* = 6$. This corresponds to the case with the highest efficiency (≈50 %) found in the study by Clark & Smits (2006). To determine the time-averaged velocity fields, DPIV data were acquired for 20 consecutive oscillation periods, with each oscillation period discretized into 30 distinct phases, resulting in a total of 600 instantaneous velocity fields obtained per case. The velocity data for all of the instantaneous fields were averaged at each point in the domain to obtain the time-averaged velocity fields.

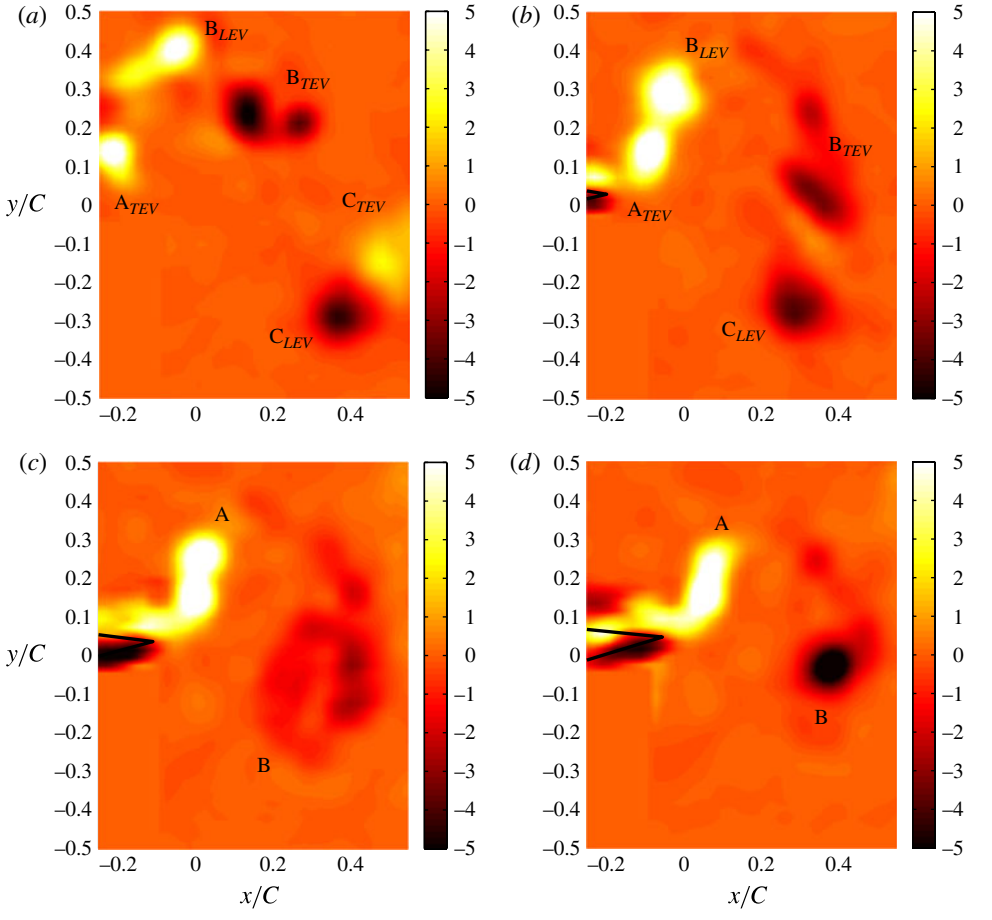

FIGURE 2. (Colour online) Vorticity fields at various spanwise locations for $St = 0.25$, $\lambda^* = 6$, and $t/T_p = 0$. (*a*) $z/S = 1$, (*b*) $z/S = 0.84$, (*c*) $z/S = 0.67$, (*d*) $z/S = 0.5$. Flow is from left to right, and the trailing edge of the fin is outlined in black.

In figure 2, the leading edge of the fin has just begun its downstroke ($t/T_p = 0$, where T_p is the oscillation period). At the midspan of the fin a reverse von Kármán vortex street is observed (figure 2*d*). The time-averaged velocity field reveals a narrow, streamwise jet indicative of thrust production (figure 3*d*). Advancing along the span towards the tip of the fin, the coherent vortex core downstream of the trailing edge at the midspan transforms and we observe a clustering of vortices (figure 2*c*) that is accompanied by a broad, high-intensity velocity jet (figure 3*c*). This cluster of vortices is formed by the amalgamation of a pair of vortices that are seen to separate with increasing spanwise extent. Figures 2(*a*) and 2(*b*) reveal a 2P wake structure that is formed by the coupling of leading edge vortices (B_{LEV} and C_{LEV}) from the previous flapping cycle with trailing edge vortices (B_{TEV} and C_{TEV}) that have the same sense of rotation being shed in the current flapping cycle. The leading and trailing edge vortices from any given flapping cycle form a vortex ring that moves by self-induction away from the centreline of the flow field, resulting in the double wake pattern seen in figures 3(*a*) and 3(*b*). This bifurcation, where both a 2S and 2P wake are observed at

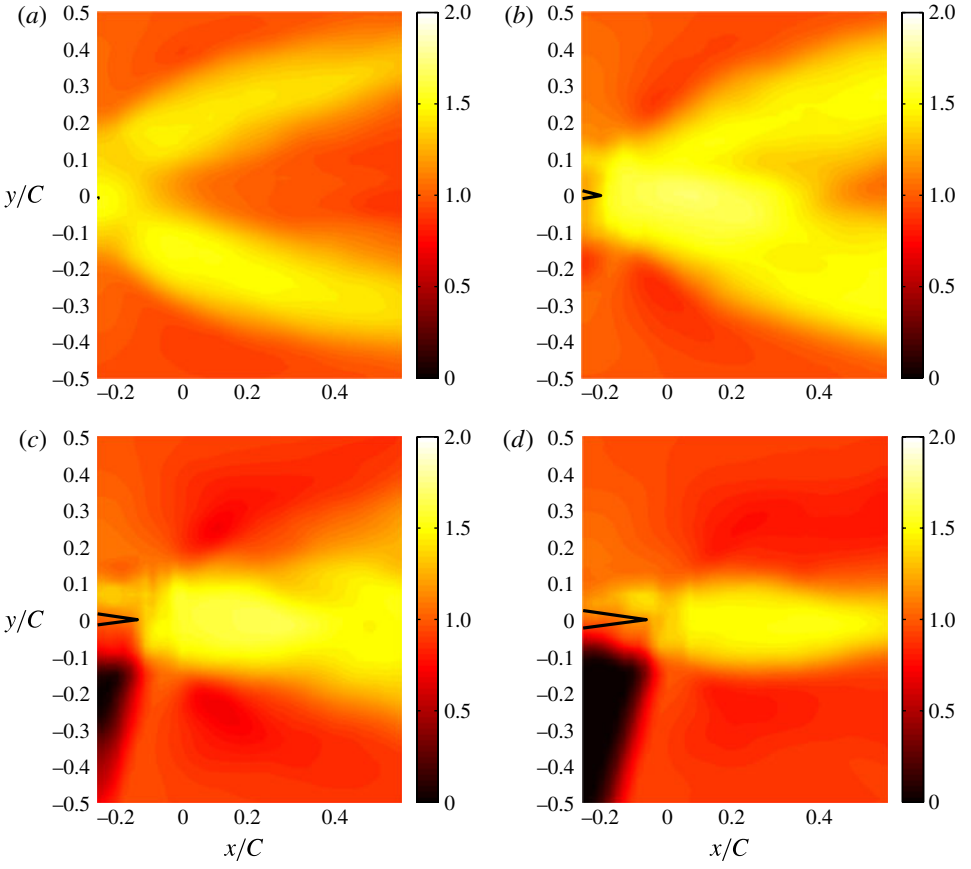

FIGURE 3. (Colour online) Time-averaged velocity fields at various spanwise locations for $St = 0.25$ and $\lambda^* = 6$. (*a*) $z/S = 1$, (*b*) $z/S = 0.84$, (*c*) $z/S = 0.67$, (*d*) $z/S = 0.5$. Flow is from left to right, and the trailing edge of the fin is outlined in black.

different spanwise locations, was also observed by Heathcote, Wang & Gursul (2008) for flexible foils where the peak-to-peak amplitude increased with span.

The relative net streamwise momentum flux for different spanwise locations can be estimated using a simple momentum balance. That is,

$$T' = \rho \int_{-\infty}^{\infty} u(y)(u(y) - U)\,\mathrm{d}y, \tag{3.1}$$

where T' is the net streamwise momentum flux per unit span, and $u(y)$ is the time-averaged velocity profile obtained from time-averaging the DPIV velocity data over 20 oscillation periods. The velocity profile selected for this analysis was located $C/4$ downstream of the trailing edge of the fin for all cases. In using (3.1) it is assumed that the incoming flow is uniform, the contribution due to transverse momentum flux is negligible, and the pressure has recovered to the free-stream pressure at the boundaries of the control volume. The validity of the latter assumptions are questionable for unsteady three-dimensional flows: Buchholz & Smits (2008) and Clark & Smits (2006) demonstrate significant spanwise flows and Green & Smits (2008) highlight time-varying pressure gradients present for three-dimensional flows. These assumptions

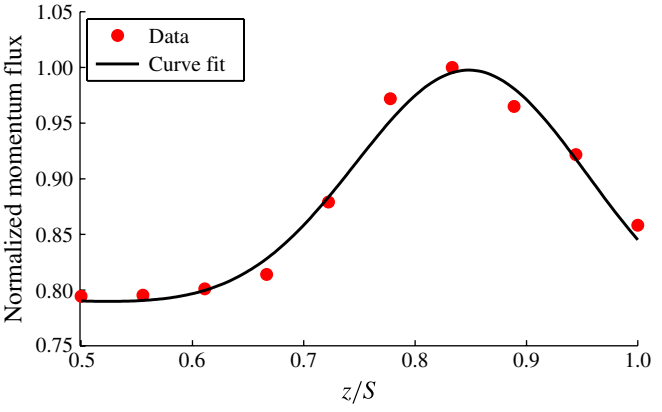

FIGURE 4. (Colour online) Net streamwise momentum flux as a function of spanwise location, normalized by maximum momentum flux value.

make the analysis susceptible to errors if the results are interpreted in the context of force generation, as pointed out by Dabiri (2005). For this reason, the results obtained using (3.1) are used only to gain a relative sense of the spanwise location where the net streamwise momentum flux is concentrated. The net thrust data were reported by Clark & Smits (2006).

The results given in figure 4 show that the net streamwise momentum flux contribution contains a peak approximately 85 % of the way down the span, and that a significant portion of the momentum flux is generated towards the tip of the fin, confirming the hypothesis made by Clark & Smits (2006). At the tip of the fin the momentum flux generation must be zero because the area reduces to zero, though this is not observed in our results due to the presence of a streamwise tip vortex that is formed beyond the tip of the fin. The induced velocity caused by this vortex results in a non-zero net streamwise momentum flux at the tip when the analysis is conducted at a finite distance downstream of the fin. The tip vortex also indicates that the spanwise transport of streamwise momentum may be significant in the wake of the fin. For comparison, the momentum flux distributions were also evaluated at a location C/2 downstream from the trailing edge of the fin and again a peak was found at a position approximately 85 % of the way along the span. Due to the limited extent of the domain, the analysis could not be conducted further downstream. Buchholz & Smits (2008) and Clark & Smits (2006) demonstrate that generally the velocity induced by tip vortices acts to compress the spanwise extent of the wake and induce spanwise flows that transport momentum from the tip towards the midspan of the fin. This spanwise transport makes it difficult to determine the exact spanwise origin of the streamwise momentum present in the wake. It appears, however, that regardless of its origin a significant portion of the net streamwise momentum flux is concentrated towards the tip of an unsteady batoid-inspired fin.

It was noted in § 1 that efficient propulsion in two dimensions occurs when the leading edge vortices coalesce with trailing edge vortices of like sign. The present case is more complex because it appears that both a 2S and 2P wake are present on a single fin. It is important to note, however, that leading and trailing edge vortices merge for a significant portion of the spanwise extent of the fin. A 2P wake structure is observed only very near the tip ($z/S > 0.8$), suggesting that efficient propulsion for

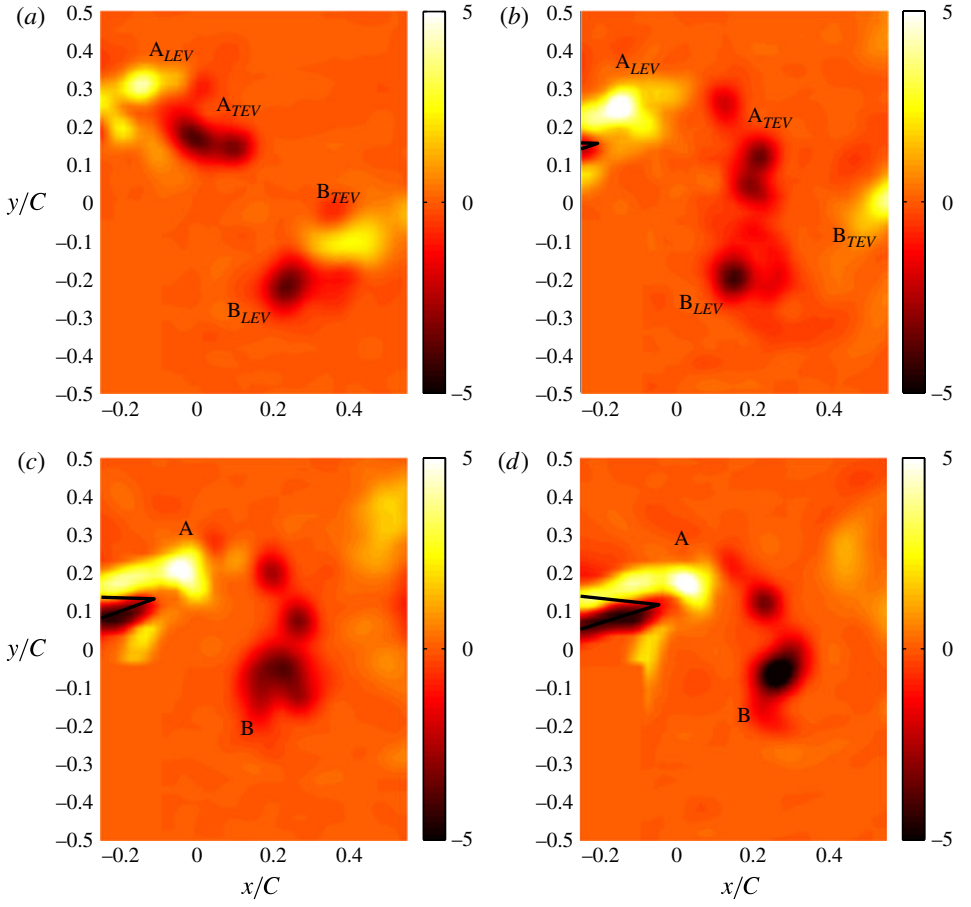

FIGURE 5. (Colour online) Vorticity fields at various spanwise locations for $St = 0.25$, $\lambda^* = 3$, and $t/T_p = 0$. (*a*) $z/S = 1$, (*b*) $z/S = 0.84$, (*c*) $z/S = 0.67$, (*d*) $z/S = 0.5$. Flow is from left to right, and the trailing edge of the fin is outlined in black.

three-dimensional flows occurs when leading edge vortices coalesce with trailing edge vortices over a significant portion of the fin.

The salient features of this wake structure appear to be insensitive to variations in the wavelength. Figure 5 shows vorticity fields for the case with $\lambda^* = 3$. Towards the tip of the fin, pairs of vortices consisting of leading edge (A_{LEV} and B_{LEV}) and trailing edge (A_{TEV} and B_{TEV}) vortices are observed in the wake (figure 5*a*,*b*). With decreasing spanwise extent, the trailing edge vortex from the current half-flapping cycle and the leading edge vortex from the previous half-flapping cycle are seen to coalesce in a manner similar to that observed in figure 2. Reducing the wavelength, however, markedly decreases the strength and extent of the vortices shed into the wake: a 17 % decrease in circulation is found for $\lambda^* = 3$ compared with $\lambda^* = 6$. Additionally, and perhaps more revealingly, a qualitative, or quantitative analysis using the Q-criterion (Hunt, Wray & Moin 1988), reveals the presence of an additional vortex core in the wake. This is seen most clearly near the midspan of the fin (figure 5*c*,*d*), where a smaller secondary vortex remains after the leading and trailing edge vortices have merged. In particular, vortex B in figure 5(*d*) consists of a pair of like-signed vortices.

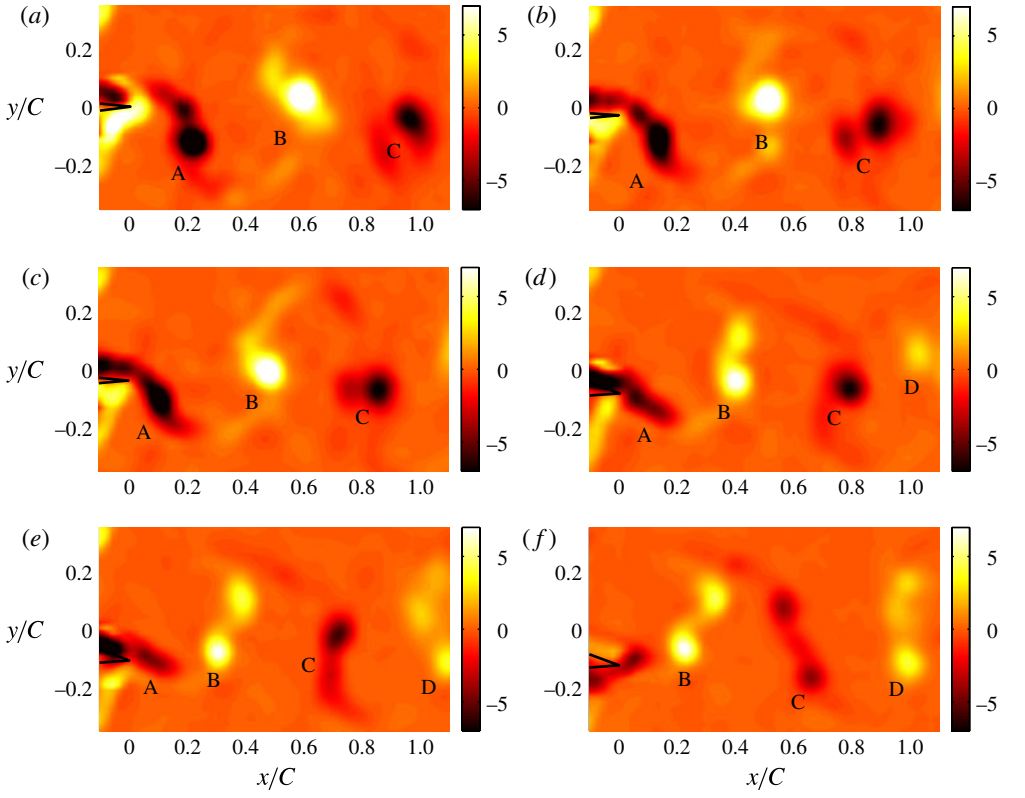

FIGURE 6. (Colour online) Vorticity fields at the midspan for different wavelengths, at $St = 0.20$ and $t/T_p = 0$. (*a*) $\lambda^* = \infty$, (*b*) $\lambda^* = 12$, (*c*) $\lambda^* = 6$, (*d*) $\lambda^* = 4$, (*e*) $\lambda^* = 3$, (*f*) $\lambda^* = 2.4$. Flow is from left to right, and the trailing edge of the fin is outlined in black.

The formation of the vortex pair appears to be entirely a trailing edge effect and not the result of pairing a leading edge and a trailing edge vortex.

This wake transition is better observed by varying the wavelength at a fixed location along the span. The results obtained at the midspan at the same instance in the flapping cycle ($t/T_p = 0$, the beginning of the downstroke of the leading edge of the fin), are shown in figure 6. With increasing λ^*, vortex B is positioned further downstream from the trailing edge of the fin. Since the leading edge of the fin is in the same part of the flapping cycle for each case shown, the difference in streamwise location of vortices between subsequent cases is due to the phase delay between the leading and trailing edges of the fin.

In conjunction with this delay in vortex shedding, it is seen that with decreasing λ^* vortex B appears to divide, or transition from a single core to a pair of vortex cores. Closer examination shows that for the longest wavelengths, $\lambda^* = \infty$, 12 and 6, the vorticity is contained entirely in a single core. A trailing vortex structure begins to emerge at $\lambda^* = 4$, before two distinct vortex cores appear at $\lambda^* = 3$ and 2.4. It is clear that the wavelength has a significant impact on the wake structure of the oscillating fin; namely, it results in a transition from a 2S to a 2P structure. This transition appears to be directly linked to the increasing phase delay of the trailing edge of the fin with respect to the leading edge as λ^* decreases.

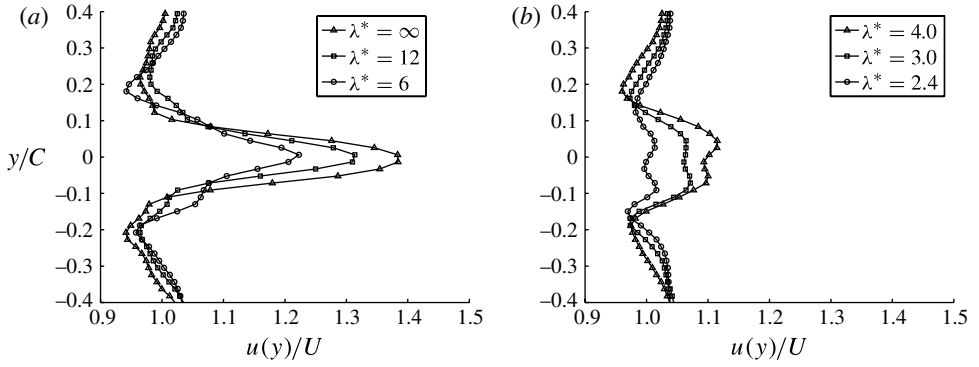

FIGURE 7. Velocity profiles at the midspan normalized by the free-stream velocity half a chord downstream of the trailing edge of the fin for various values of λ^*; $St = 0.25$. (*a*) Higher λ^* where a 2S wake was observed, (*b*) lower λ^* where a 2P wake was observed.

As seen in figure 6, with decreasing λ^* there is a monotonic and significant decrease in the strength of the vorticity shed into the wake. The peak vorticity captured within a vortex core revealed a decrease of 43 % when λ^* decreases from ∞ to 2.4. A reverse von Kármán vortex street results in a jet-like average flow, and we would expect that an increase in vortex strength would result in a stronger jet profile. Hence, it might be expected that the purely heaving motion, $\lambda^* = \infty$, would yield a jet with the highest momentum flux, and this is confirmed by the results displayed in figure 7. For $St = 0.25$ it is seen that the time-averaged wake takes the form of a jet profile for all wavelengths. There is a monotonic decrease in the peak jet velocity obtained with decreasing λ^*, and thus a corresponding decrease in the momentum flux per unit span, T', as defined by (3.1). In addition, the presence of a pair of vortices in the wake for $\lambda^* = 4$, 3, and 2.4 result in a double wake structure where the time-averaged streamwise velocity profiles display two peaks.

4. Effects of Strouhal number

Here we discuss the results obtained for different Strouhal numbers at a fixed λ^*, that is, $\lambda^* = 6$. Vorticity fields at various spanwise locations for $St = 0.35$ are shown in figure 8. The differences between this case and the case with the highest efficiency shown in figure 2 are somewhat subtle. Despite a significant increase in vortex strength (57 %), the dominant wake structures remain: a 2S structure is observed at the midspan that branches to form a 2P structure towards the tip, although the branching of the vortex core occurs closer to the midspan with increasing Strouhal number. The data suggests that the bifurcation occurs at $z/S \approx 0.75$ for this case as opposed to $z/S \approx 0.8$ for the higher-efficiency case. The streamwise distance between shed vortex rings (composed of both a leading and trailing edge vortex) decreases with increasing Strouhal number.

Figure 9 shows the vorticity fields at the midspan of the fin for a range of Strouhal numbers. The lowest Strouhal number examined here did not produce coherent vortex cores, but rather a sinusoidally varying vortex sheet (figure 9*a*). This observation agrees with that by Anderson *et al.* (1998), who showed that below a certain threshold the unsteadiness of the oscillating fin is insufficient to promote the instability leading to vortex roll-up. The first manifestation of an unsteady vortex wake occurs at $St = 0.15$, and somewhat surprisingly it is a 2P wake structure, where a pair of

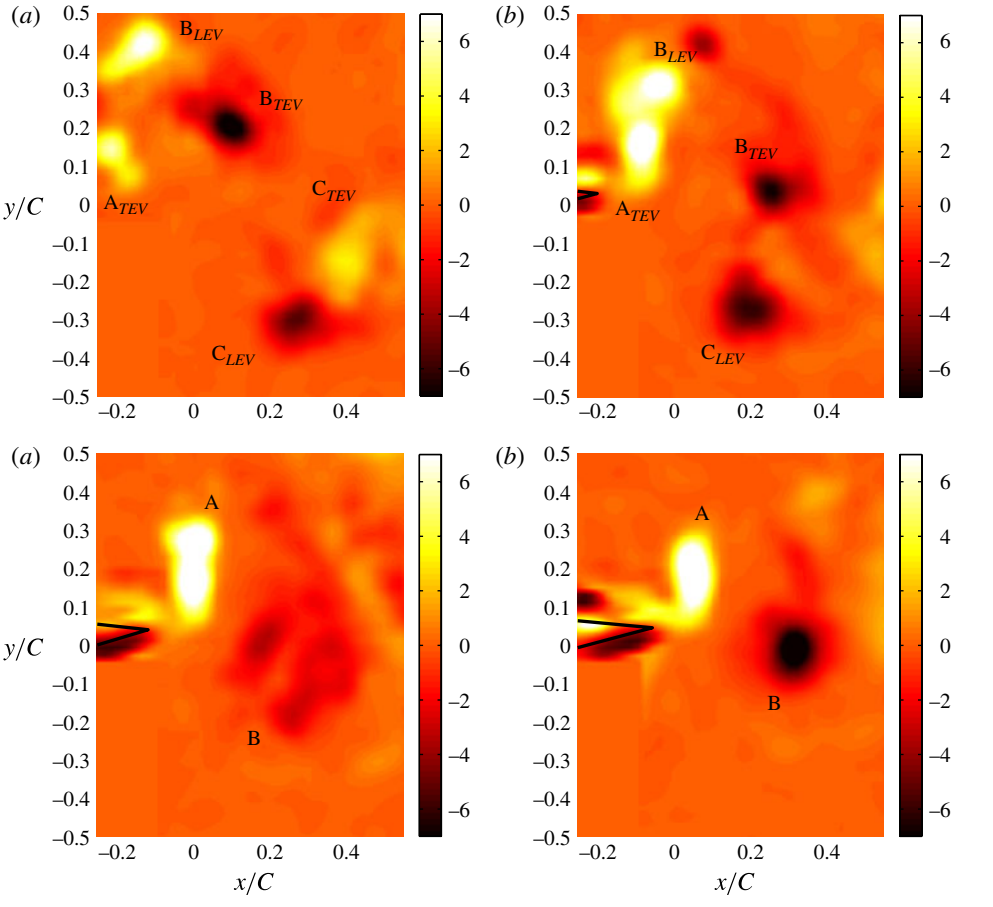

FIGURE 8. (Colour online) Vorticity fields at various spanwise locations for $St = 0.35$, $\lambda^* = 6$, and $t/T_p = 0$. (*a*) $z/S = 1$, (*b*) $z/S = 0.84$, (*c*) $z/S = 0.67$, (*d*) $z/S = 0.5$. Flow is from left to right, and the trailing edge of the fin is outlined in black.

vortices is created every half-flapping cycle (figure 9*b*). Increasing the Strouhal number beyond ∼0.2 produces a 2S vortex structure (figure 9*c–f*). Williamson & Roshko (1988) discovered a similar change in structure at low Strouhal numbers in the wake of an oscillating cylinder, and Schnipper *et al.* (2009) found similar results for a pitching foil.

These results, combined with the observations presented in § 3, where a transition from 2S to 2P was observed by varying the wavelength, indicate that for a given Strouhal number (or non-dimensional wavelength), there is a specific non-dimensional wavelength (or Strouhal number) such that a transition from a 2S to 2P wake structure occurs. It is important to note that a transition from 2P to 2S always occurs with increasing Strouhal number, as highlighted in figure 10.

Increasing the Strouhal number increases the strength of the shed vortices. It also decreases the time between vortex shedding events, thereby decreasing the streamwise distance between subsequent vortices. Vortex interactions therefore play an ever-increasing role with increasing Strouhal number. This effect can become so pronounced that the vortices furthest downstream from the trailing edge of the fin

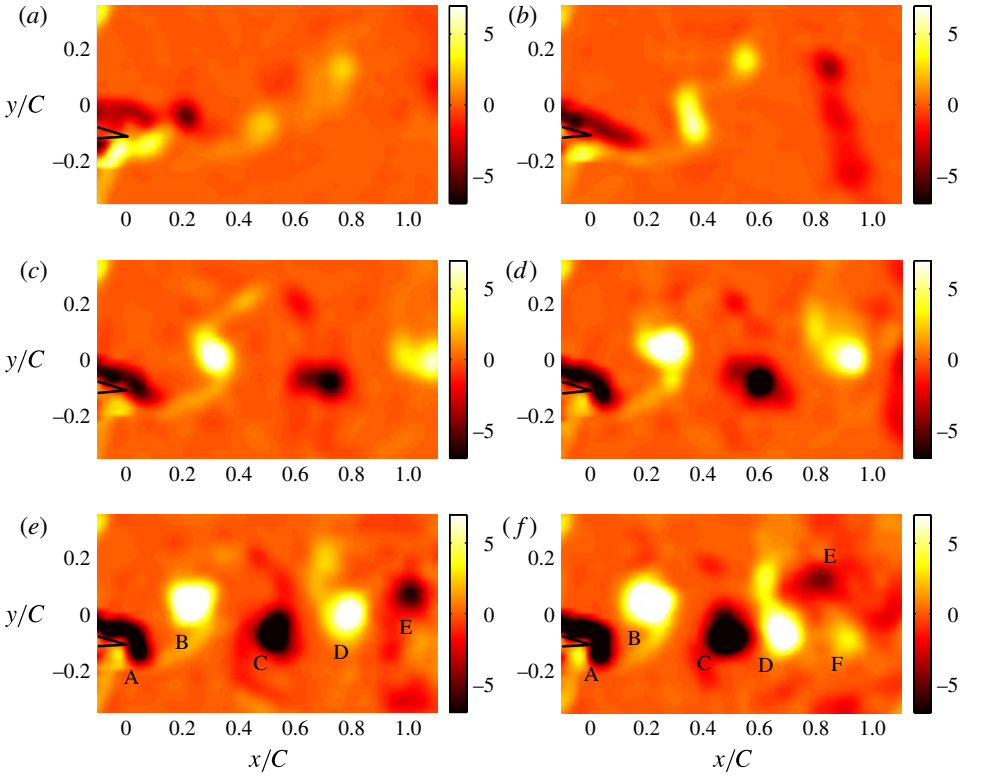

FIGURE 9. (Colour online) Vorticity fields at the midspan for various Strouhal numbers, $\lambda^* = 6$ and $t/T_p = 0$. (*a*) $St = 0.1$, (*b*) $St = 0.15$, (*c*) $St = 0.2$, (*d*) $St = 0.25$, (*e*) $St = 0.3$, (*f*) $St = 0.35$. Flow is from left to right, and the trailing edge of the fin is outlined in black.

are seen to cross over the line of symmetry in the wake. For example, at $St = 0.35$, the first two pairs of vortex cores are aligned in a reverse von Kármán vortex street, whereas vortices C and D are aligned so that the induced velocity between the pair opposes the free-stream velocity (figure 9*f*). The time evolution of this phenomenon indicates that the vortex labelled C starts below the line of symmetry at $t/T_p = 0$ and is induced above the line of symmetry at $t/T_p = 0.75$ (figure 11).

The mean velocity profiles taken half a chord downstream of the trailing edge are shown in figure 12. For $St = 0.10$ and 0.15 a deficit profile is observed, but for higher Strouhal numbers a jet with increasing levels of momentum flux develops, flanked on either side by a small deficit profile. This result was also observed by Lewin & Haj-Hariri (2003), where it was noted that the qualitative shape of the velocity profiles had a significant impact on the stability of the corresponding jet. This connection between the velocity profile and the wake structure is currently under investigation using linear spatial stability analysis (Moored, private communication).

5. Wake bifurcations and scaling

If the velocity profiles of figure 12 were displayed at a different location downstream of the fin, significantly different conclusions might be drawn from the results. To better understand how the velocity profile varies with streamwise location, time-averaged velocity fields were examined in figure 13. A coherent jet structure for

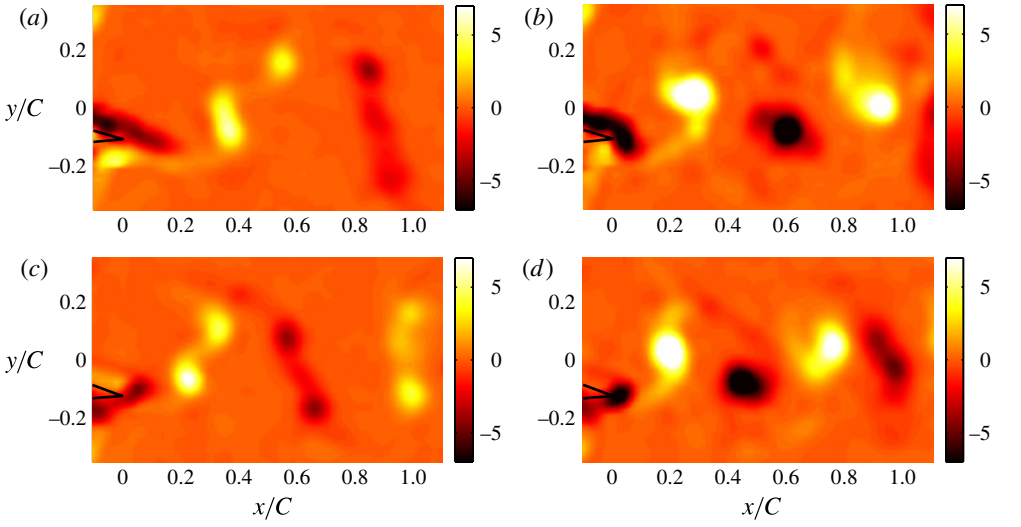

FIGURE 10. (Colour online) Wake transition from 2P to 2S with increasing Strouhal number at the midspan. (*a*) $\lambda^* = 6$, $St = 0.15$, (*b*) $\lambda^* = 6$, $St = 0.25$, (*c*) $\lambda^* = 2.4$, $St = 0.2$ (*d*) $\lambda^* = 2.4$, $St = 0.3$. Flow is from left to right, and the trailing edge of the fin is outlined in black.

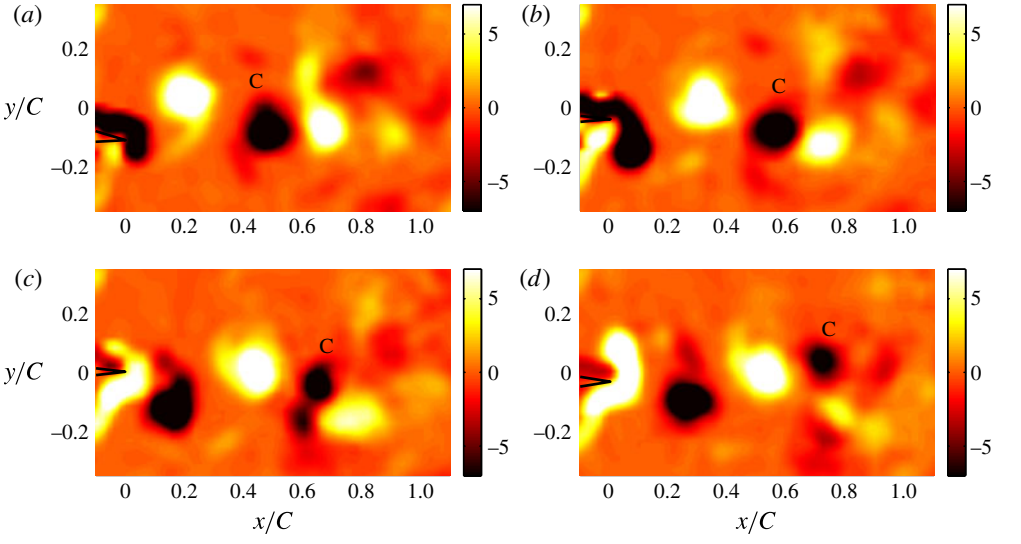

FIGURE 11. (Colour online) Vorticity fields at the midspan for $St = 0.35$ and $\lambda^* = 6$ at various stages in the flapping cycle. (*a*) $t/T_p = 0$, (*b*) $t/T_p = 0.25$, (*c*) $t/T_p = 0.5$, (*d*) $t/T_p = 0.75$. Flow is from left to right, and the trailing edge of the fin is outlined in black.

the moderate Strouhal numbers ($St = 0.2$ and 0.25) is observed, but at the highest Strouhal numbers ($St = 0.3$ and 0.35) the jet bifurcates into a pair of jets at a finite distance downstream of the fin. When comparing the vorticity fields of figure 9 to the velocity fields of figure 13, it can be seen that the 2S reverse von Kármán vortex street of $St = 0.2$ and 0.25 time-averages into a single coherent jet profile. The enhanced

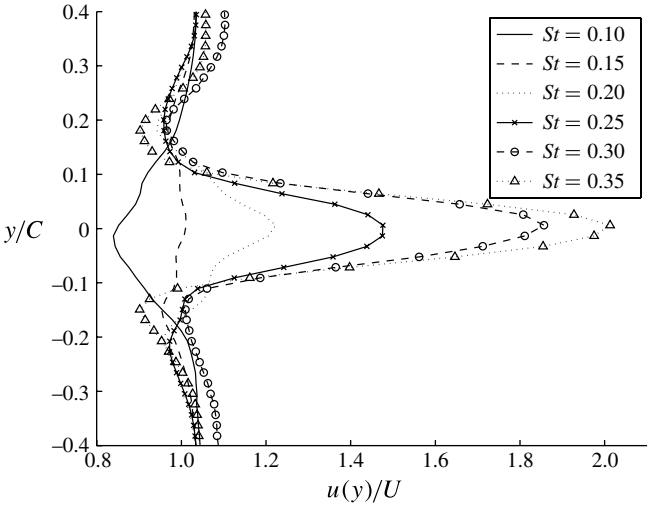

FIGURE 12. Velocity profiles at the midspan half a chord downstream of the trailing edge of the fin for various Strouhal numbers, $\lambda^* = 6$.

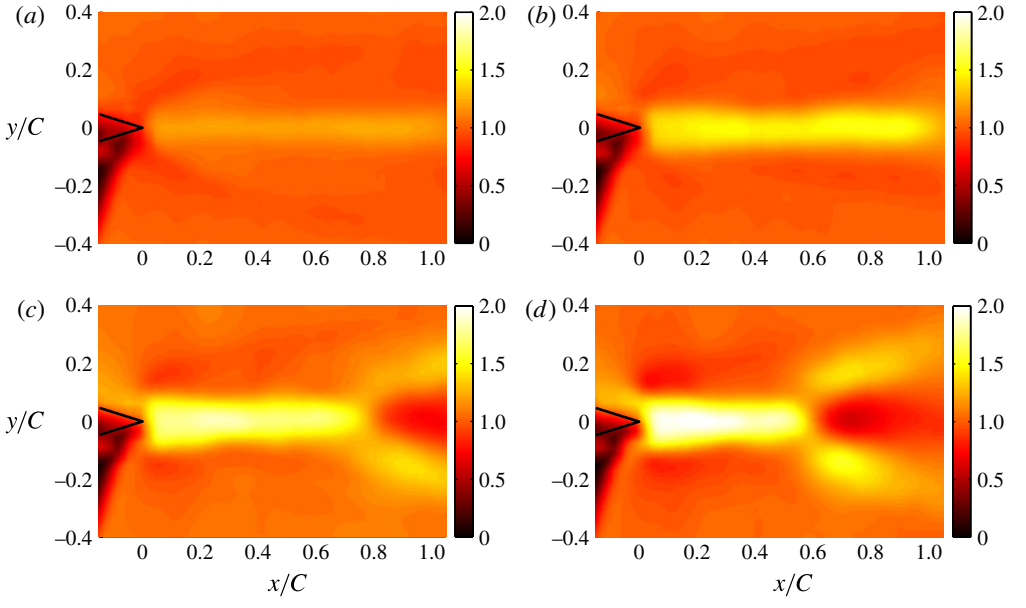

FIGURE 13. (Colour online) Time-averaged velocity fields at the midspan for various Strouhal numbers, with $\lambda^* = 6$. (*a*) $St = 0.2$, (*b*) $St = 0.25$, (*c*) $St = 0.3$, (*d*) $St = 0.35$. Flow is from left to right.

complexity of the vortical patterns in the wake of the highest Strouhal numbers, whereby vortex cores are seen to cross the plane of symmetry (figure 11), signals the transition from a single to double wake structure. At the streamwise location where the vortices cross the line of symmetry, the time-averaged velocity fields indicate a wake bifurcation.

Similar results were observed for a rigid pitching panel (Buchholz & Smits 2006), for a pitching and heaving elliptical aerofoil (Dong *et al.* 2006), and for anguilliform swimmers (Borazjani & Sotiropoulos 2008). Since the high-velocity jets are formed at an acute angle to the streamwise direction, the wake bifurcations direct momentum transverse to the streamwise direction. While the net streamwise momentum flux increases monotonically with Strouhal number (figure 12), the ratio of streamwise to transverse momentum flux is reduced due to the bifurcation. This leads to a decrease in the propulsive efficiency with increasing Strouhal number since a greater portion of the total momentum flux generated is transverse to the direction of forward motion (Buchholz & Smits 2006; Dong *et al.* 2006; Clark & Smits 2006). Preliminary results from a linear spatial stability analysis also suggests that the bifurcation point might be closely related to wake resonance and efficiency, but further studies are needed to fully resolve this issue (Moored, private communication).

To see how the bifurcation depends on Strouhal number, additional measurements were taken at $Re_C = 8100$. The bifurcation distance X_{bi} was found by examining the velocity fields. The angle θ_{bi} that the bifurcation makes with the symmetry line was estimated by drawing a straight line through the local maxima in the mean streamwise velocity. Due to system limitations the furthest downstream that a bifurcation could be identified was 1.15 chords from the trailing edge. The errors in X_{bi} and θ_{bi} are estimated to be 5–10 % and 10–15 %, respectively.

The bifurcation distance decreases with increasing Strouhal number and increases with decreasing wavelength (figure 14). These results are not surprising in light of the discussions of §§ 3 and 4, where it was noted that a monotonic increase in vorticity strength was observed for increasing λ^* and Strouhal number. The results of Dong *et al.* (2006), Buchholz & Smits (2006) and the current study suggest that the wake bifurcates when the vortex rings produced by the fin are sufficiently strong to self-induce themselves away from the symmetry line of the flow field. Thus, we expect, and do in fact see, that the parameters leading to an increase in vorticity strength also decrease the wake bifurcation distance.

In light of this, a scaling of the bifurcation data is sought. The scaling suggested here is similar to that used by Green & Smits (2008) and it is based on concepts derived from finite wing theory, where the lift shows a strong dependence on aspect ratio. Green & Smits (2008) successfully scaled the coefficients of pressure and thrust using a linear function of the aspect-ratio and pitching amplitude to chord ratio. Since the bifurcation distance in figure 14(*a*) depends on λ^* and St, a scaling is sought in the following form:

$$X^*_{bi} = \frac{X_{bi}}{C}[1 + f(\lambda^*)]. \tag{5.1}$$

These results suggest a monotonically decreasing scaling with λ^*; thus a linear form for f is assumed, so that

$$X^*_{bi} = \frac{X_{bi}}{C}[1 + \kappa(1/\lambda^*)]. \tag{5.2}$$

With the scaling in (5.2) and a value of $\kappa = -1$, figure 14(*b*) shows that the data collapses onto a single curve. As noted in § 2, the fin causes a small blockage of the water channel (2.8 %) that could accelerate the fluid and distort the flow field. These pressure gradients may affect the value of κ in (5.2) (that is, κ could be facility-dependent).

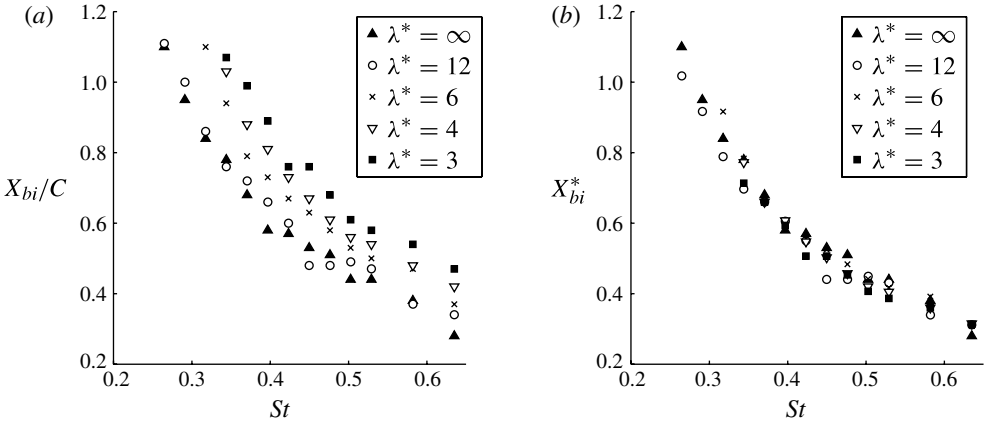

FIGURE 14. Bifurcation distance as a function of Strouhal number at the midspan. (*a*) Unscaled data, (*b*) scaled data using (5.2) with $\kappa = -1$.

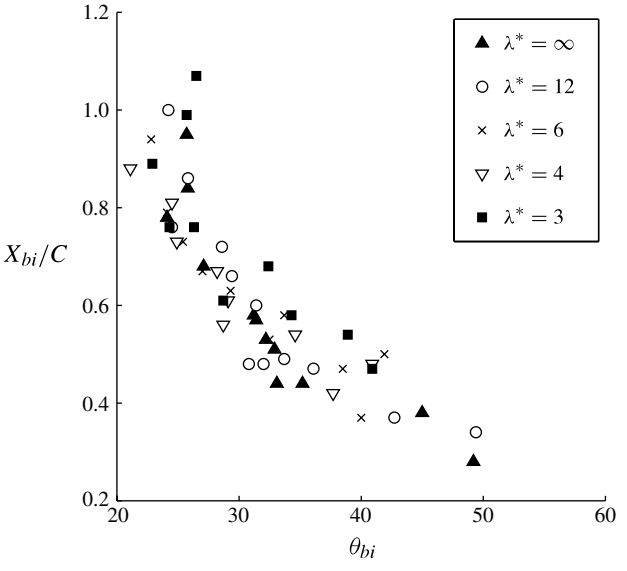

FIGURE 15. Bifurcation distance as a function of the angle of the resulting jet.

In figure 15 we plot the bifurcation distance, X_{bi}, as a function of the bifurcation angle, θ_{bi}. Though there is considerable scatter in the data, it appears as though the bifurcation angle is independent of the wavelength, suggesting that the angle depends solely on the bifurcation distance. For the data presented here, the bifurcation angle tends towards a value of $\sim 25^\circ$ for the largest bifurcation distances. In comparison with past results, Dong *et al.* (2006) determined a bifurcation angle of 20° for an elliptical planform fin with an aspect ratio of 1.27 undergoing a pitching and heaving motion, which is encouragingly close to our result.

The wake bifurcation presented may be the three-dimensional realization of the two-dimensional asymmetric wakes described by Godoy-Diana *et al.* (2009). Their model, based on the self-advection of a dipolar vortex structure formed from

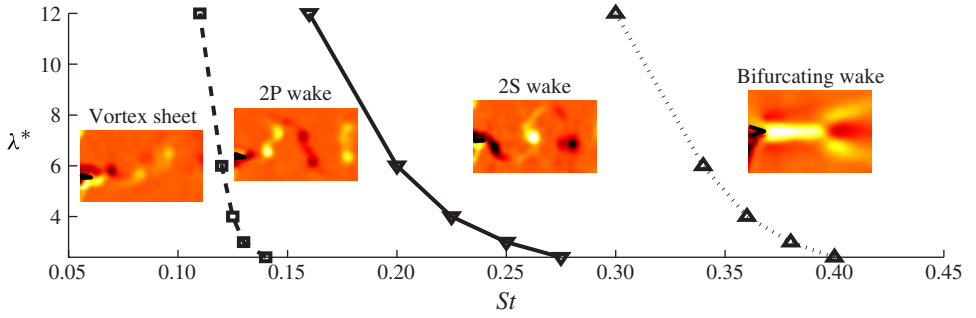

FIGURE 16. (Colour online) Transitions in the wake of a batoid-inspired oscillating fin at the midspan in the λ^* versus St map. Dashed line – approximate transition from sinusoidally varying vortex sheet to 2P wake; Solid line – transition from 2P to 2S wake; Dotted line – point where wake bifurcation occurs one chord length from the trailing edge of the fin.

successive vortices shed from the fin, predicts the symmetry-breaking tendencies of two-dimensional wakes. To perform a similar analysis in the three-dimensional flows studied here, the self-advection of vortex rings composed of leading edge, tip, and trailing edge vortices would need to be considered to determine if there exists a critical induced velocity resulting in a wake bifurcation. Such an analysis is beyond the scope of the current work.

6. Concluding remarks

The wake structure of a batoid-inspired oscillating fin was found to depend strongly on wavelength and Strouhal number. The wake structures and transitional points at the midspan of the fin are summarized in the (λ^*, St) phase space in figure 16. As an example of the general trend in wake transitions observed in the study, for $\lambda^* = 6$, the lowest Strouhal numbers (0.1–0.125) did not produce coherent vortex cores in the fin wake but rather a wavy vortex sheet. A slight increase in Strouhal number promoted the creation of a 2P wake structure (0.15–0.2) before giving way to a 2S wake structure at higher Strouhal numbers. This 2P-to-2S transition was delayed with decreasing wavelength; for instance at $\lambda^* = 2.4$ this transition is only observed for $St \geqslant 0.25$. In all cases, the transition from 2P to 2S occurs with decreasing oscillation period, indicating that a formation number analysis (Dabiri 2009) may be applicable. Although this analysis is not possible on the current data set due to limitations in both spatial (particularly in the near-wake of the fin) and temporal resolution, recent work by Buchholz, Green & Smits (2011) suggests a more generalized formation number that applies to unsteady three-dimensional flows. This new parameter is defined by the vortex circulation scaled by a dynamic pressure associated with the maximum transverse velocity of the trailing edge. Their study of rigid pitching panels of different aspect ratios show a qualitative trend in wake structure leading to the 2S-to-2P transition similar to that seen in the current effort, suggesting that this transition may be governed by a vortex pinch-off process.

Increasing the Strouhal number causes an increase in the strength of the vortices being shed and a decrease in the streamwise distance between subsequent vortices. The combined effect is to cause the wake to bifurcate at a finite distance downstream of the fin. The splitting of the wake occurs at an acute angle to the streamwise direction and results in a decrease in efficiency due to the reduction in the ratio

between streamwise and transverse momentum flux. Wake bifurcations of this nature appear to be the result of three-dimensional effects. Two-dimensional studies, for instance Lewin & Haj-Hariri (2003) and Godoy-Diana *et al.* (2009), suggest that an increase in Strouhal number yields an asymmetric wake. This highlights a fundamental difference in two and three-dimensional flows, whereby three-dimensionality stabilizes the asymmetries that prevail in two-dimensional flows.

The non-dimensional wavelength, λ^*, proved to be an important factor governing the transition from 2P to 2S wake structures at the midspan of the fin, and the nature of the wake bifurcation. As λ^* increases, the relative instantaneous angle of attack of the fin increases, resulting in an increase in the subsequent vortex strength shed into the wake of the fin. This implies that a purely heaving motion, $\lambda^* = \infty$, results in the strongest vortices in the wake that time-average to create velocity jets containing the most momentum. However, the increased vortex strength comes at a cost. Wake bifurcation, which can lead to a decrease in efficiency, is promoted by an increase in vortex strength. It was found that the wake bifurcation first occurs for $\lambda^* = \infty$ at a relatively low Strouhal number, and the bifurcation distance from the trailing edge of the fin monotonically increases with decreasing λ^*. A simple linear scaling was found to collapse the bifurcation distance as a function of Strouhal number for all wavelengths examined here.

The most prominent features of the wake at various spanwise locations were similar for all cases examined. Although the classification of the wake structure as either 2S or 2P at the midspan depends on λ^* and Strouhal number, the splitting of the leading and trailing edge vortices to form a double wake structure with increasing spanwise location was common to all cases. At the midspan of the fin, leading and trailing edge vortices combined to form a reverse von Kármán vortex street. The leading and trailing edge vortices were found to branch with increasing spanwise extent, so that at the tip of the fin a double wake structure consisting of pairs of leading and trailing edge vortices was observed. At the point where the splitting of the leading and trailing edge vortices occurred, a broad high-intensity velocity jet was created that provided a significant contribution to the overall streamwise momentum developed by the fin.

Clark & Smits (2006) report a maximum in efficiency of $\sim$50 % for $St = 0.25$ and $\lambda^* \approx 4$–6 for a similar experimental setup. In the context of the present work, this suggests that efficiency is maximized when a 2S wake structure is present at the midspan of the fin that does not bifurcate within one chord length downstream of the fin. A small increase in either Strouhal number or wavelength yields a bifurcating wake that is less efficient, and a decrease in either Strouhal number or wavelength yields a 2P wake structure that is also less efficient. It appears that there exists a small window of the most efficient operation where the leading and trailing edge vortices coalesce to form a 2S wake structure at the midspan that does not bifurcate in the near-wake region of the fin.

Acknowledgements

D. Rein-Weston and D. Quinn helped to design and construct some aspects of the experimental apparatus, and Drs M. Green, M. Leftwich, and K. Moored gave freely of their time to discuss the various aspects of the project. This work was supported by the Office of Naval Research under Program Director Dr B. Brizzolara, MURI grant number N00014-08-1-0642.

REFERENCES

ANDERSON, J. M., STREITLIEN, K., BARRETT, D. S. & TRIANTAFYLLOU, M. S. 1998 Oscillating foils of high propulsive efficiency. *J. Fluid Mech.* **360**, 41–72.

BLONDEAUX, P. O., FORNARELLI, F., GUGLIELMINI, L., TRIANTAFYLLOU, M. S. & VERZICCO, M. 2005 Numerical experiments on flapping foils mimicking fish-like locomotion. *Phys. Fluids* **17**, 113601.

BORAZJANI, I. & SOTIROPOULOS, F. 2008 Numerical investigation of the hydrodynamics of carangiform swimming in the transitional and inertial flow regimes. *J. Expl Biol.* **211**, 1541–1558.

BUCHHOLZ, J. H. J., GREEN, M. A. & SMITS, A. J. 2011 Scaling the circulation shed by a pitching panel. *J. Fluid Mech.* **688**, 591–601.

BUCHHOLZ, J. H. J. & SMITS, A. J. 2006 On the evolution of the wake structure produced by a low-aspect-ratio pitching panel. *J. Fluid Mech.* **546**, 433–443.

BUCHHOLZ, J. H. J. & SMITS, A. J. 2008 The wake structure and thrust performance of a rigid low-aspect-ratio pitching panel. *J. Fluid Mech.* **603**, 331–365.

CHAN, A. S., DEWEY, P. A., JAMESON, A., LIANG, C. & SMITS, A. J. 2011 Vortex suppression and drag reduction in the wake of counter-rotating cylinders. *J. Fluid Mech.* **679**, 343–382.

CLARK, R. P. & SMITS, A. J. 2006 Thrust production and wake structure of a batoid-inspired oscillating fin. *J. Fluid Mech.* **562**, 415–429.

DABIRI, J. O. 2005 On the estimation of swimming and flying forces from wake measurements. *J. Expl Biol.* **208**, 3519–3532.

DABIRI, J. O. 2009 Optimal vortex formation as a unifying principle in biological propulsion. *Annu. Rev. Fluid Mech.* **41**, 17–33.

DABIRI, J. O. & GHARIB, M. 2005 Starting flow through nozzles with temporally variable exit diameter. *J. Fluid Mech.* **538**, 111–136.

DONG, H., MITAL, R. & NAJJAR, F. M. 2006 Wake topology and hydrodynamic performance of low-aspect-ratio flapping foils. *J. Fluid Mech.* **566**, 309–343.

DRUCKER, E. G. & LAUDER, G. V. 1999 Locomotor forces on a swimming fish: three-dimensional vortex wake dynamics quantified using particle image velocimetry. *J. Fluid Mech.* **202**, 2392–2412.

VON ELLENRIEDER, K. D., PARKER, K. & SORIA, J. 2003 Flow structures behind a heaving and pitching finite-span wing. *J. Fluid Mech.* **490**, 129–138.

GHARIB, M., RAMBOD, E. & SHARIFF, K. 1998 A universal time scale for vortex ring formation. *J. Fluid Mech.* **360**, 121–140.

GODOY-DIANA, R., AIDER, J. L. & WESFREID, J. E. 2008 Transitions in the wake of a flapping foil. *Phys. Rev.* E **77**, 016308.

GODOY-DIANA, R., MARAIS, C., AIDER, J. L. & WESFREID, J. E. 2009 A model for the symmetry breaking of the reverse Bénard–von Kármán vortex street produced by a flapping foil. *J. Fluid Mech.* **622**, 23–32.

GREEN, M. A. & SMITS, A. J. 2008 Effects of three-dimensionality on thrust production by a pitching panel. *J. Fluid Mech.* **615**, 211–220.

GUGLIELMINI, L. & BLONDEAUX, P. 2004 Propulsive efficiency of oscillating foils. *Euro. J. Fluid Mech.* **23**, 255–278.

HEATHCOTE, S., WANG, Z. & GURSUL, I. 2008 Effect of spanwise flexibility on flapping wing propulsion. *J. Fluids Struct.* **24**, 183–199.

HEINE, C. 1992 Mechanics of flapping fin locomotion in the cownose ray, Rhinoptera bonasus (Elasmobranchii: Myliobatidae). PhD thesis, Duke University, Durham, NC, USA.

HULTMARK, M., LEFTWICH, M. & SMITS, A. J. 2007 Flowfield measurements in the wake of a robotic lamprey. *Exp. Fluids* **43**, 683–690.

HUNT, J. C. R., WRAY, A. A. & MOIN, P. 1988 Eddies, streams, and convergence zones in turbulent flows. *Center for Turbulence Research Rep.* CTR-S88.

JEON, D. & GHARIB, M. 2004 On the relationship between the vortex formation process and cylinder wake patterns. *J. Fluid Mech.* **519**, 161–181.

JIMÉNEZ, J. M. 2002 Low Reynolds number studies in the wake of a submarine model using particle image velocimetry. Master's thesis, Princeton University, Princeton, NJ, USA.

KOOCHESFAHANI, M. M. 1989 Vortical patterns in the wake of an oscillating aerofoil. *AIAA Journal* **27**, 1200–1205.

LENTINK, D., MUIJRES, F. T., DONKER-DUYVIS, F. J. & VAN LEEUWEN, J. L. 2008 Vortex wake interactions of a flapping foil that models animal swimming and flight. *J. Expl Biol.* **211**, 267–273.

LEWIN, G. C. & HAJ-HARIRI, H. 2003 Modelling thrust generation of a two-dimensional heaving aerofoil in a viscous flow. *J. Fluid Mech.* **492**, 339–362.

MILANO, M. & GHARIB, M. 2005 Uncovering the physics of flapping flat plates with artificial evolution. *J. Fluid Mech.* **534**, 403–409.

RAFFEL, M., WILLERT, C. & KOMPENHANS, J. 1998 *Particle Image Velocimetry*. Springer.

ROSENBERGER, L. 2001 Pectoral fin locomotion in batoid fishes: undulation versus oscillation. *J. Expl Biol.* **204**, 379–394.

SCHAEFER, J. & SUMMERS, A. 2005 Batoid wing skeletal structure: novel morphologies, mechanical implications, and phylogenetic patterns. *J. Morphol.* **264**, 298–313.

SCHNIPPER, T., ANDERSEN, A. & BOHR, T. 2009 Vortex wakes of a flapping foil. *J. Fluid Mech.* **633**, 411–423.

TAYLOR, G. K., NUDDS, R. L. & THOMAS, A. L. R. 2003 Flying and swimming animals cruise at a Strouhal number tuned for high power efficiency. *Nature* **435**, 707–711.

TRIANTAFYLLOU, G. S., TRIANTAFYLLOU, M. S. & GROSENBAUGH, M. A. 1993 Optimal thrust development in oscillating foils with application to fish propulsion. *J. Fluids Struct.* **7**, 205–224.

TRIANTAFYLLOU, M. S., TRIANTAFYLLOU, G. S. & GOPALKRISHNAN, R. 1991 Wake mechanics for thrust generation in oscillating foils. *Phys. Fluids* **3** (12), 2835–2837.

TYTELL, E. D. & LAUDER, G. V. 2004 The hydrodynamics of eel swimming. Part I. Wake structure. *J. Expl Biol.* **207**, 1825–1841.

WALKER, J. A. & WESTNEAT, M. W. 2002 Performance limits of labriform propulsion and correlates with fin shape and motion. *J. Expl Biol.* **205**, 177–187.

WILLIAMSON, C. H. K. & ROSHKO, A. 1988 Vortex formation in the wake of an oscillating cylinder. *J. Fluids Struct.* **2**, 355–381.